Neuron

Article

p16-expressing microglia and endothelial cells promote tauopathy and neurovascular abnormalities in *PS19* mice

Graphical abstract

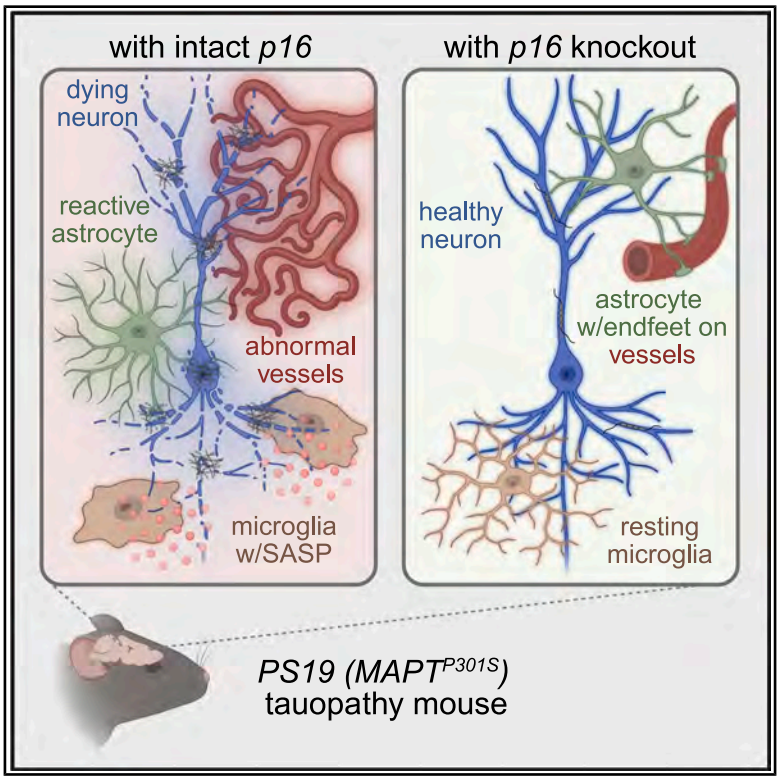

Highlights

- Genetic ablation of *p16^{Ink4a}* attenuates disease phenotypes in PS19 tauopathy mice
- PS19 mice exhibit neurovascular abnormalities that correlate with disease severity
- *p16^{Ink4a}* deletion in endothelial cells and microglia alone attenuates tau disease

Authors

Sara I. Graves, Charlton F. Meyer, Karthik B. Jeganathan, Darren J. Baker

Correspondence

baker.darren@mayo.edu

In brief

Graves et al. show that loss of an important cell-cycle inhibitor, *p16^{Ink4a}*, prevents multiple signs of neurodegenerative disease in a mouse model of tauopathy. The authors also show that *p16^{Ink4a}* expression in two specific brain cell types, endothelial cells and microglia, promotes tau-based disease.

Graves et al., 2025, Neuron *113*, 2251–2264
July 23, 2025
https://doi.org/10.1016/j.neuron.2025.04.020

CellPress

Neuron

CellPress

Article

p16-expressing microglia and endothelial cells promote tauopathy and neurovascular abnormalities in *PS19* mice

Sara I. Graves,[1] Charlton F. Meyer,[1] Karthik B. Jeganathan,[1] and Darren J. Baker[1,2,3,4,5,*]
[1]Department of Pediatric and Adolescent Medicine, Mayo Clinic, 200 1st ST., Rochester, MN 55905, USA
[2]Department of Biochemistry and Molecular Biology, Mayo Clinic, 200 1st ST., Rochester, MN 55905, USA
[3]Paul F. Glenn Center for Biology of Aging Research, Mayo Clinic, 200 1st ST., Rochester, MN 55905, USA
[4]Robert and Arlene Kogod Center on Aging, Mayo Clinic, 200 1st ST., Rochester, MN 55905, USA
[5]Lead contact
*Correspondence: baker.darren@mayo.edu
https://doi.org/10.1016/j.neuron.2025.04.020

SUMMARY

Cellular senescence is characterized by irreversible cell-cycle exit, a pro-inflammatory secretory phenotype, macromolecular damage, and deregulated metabolism. Senescent cells are highly associated with age-related diseases. We previously demonstrated that targeted elimination of senescent cells prevents neurodegenerative disease in tau (*MAPT*^{P301S};*PS19*) mutant mice. Here, we show that genetic ablation of the senescence mediator *p16*^{Ink4a} is sufficient to attenuate senescence signatures in *PS19* mice. Disease phenotypes—including neuroinflammation, phosphorylated tau, neurodegeneration, and cognitive impairment—were blunted in the absence of *p16*^{Ink4a}. Additionally, we found that *PS19* mouse brains display *p16*^{Ink4}-dependent neurovascular alterations such as vessel dilation, increased vessel density, deregulated endothelial cell extracellular matrix, and astrocytic endfoot depolarization. Finally, we show that *p16*^{Ink4a} deletion in endothelial cells and microglia alone attenuates many of the same phenotypes. Altogether, these results indicate that neurodegenerative disease in *PS19* mice is driven, at least in part, by *p16*^{Ink4a}-expressing endothelial cells and microglia.

INTRODUCTION

Organismal aging is generally described as the progressive decline in physiological function with time, which is marked by increased predisposition to disease.[1] Medical advancements that permit individuals to live longer are increasing the size of the world's geriatric population. Thus, there is greater effort to mechanistically understand the age-related basis for susceptibility to a myriad of diseases, including cardiovascular disease, cancer, and neurodegenerative disease. In recent years, many studies have suggested that cellular senescence may be a key node linking age-related tissue dysfunction and disease.[2] Senescent cells are irreversibly growth arrested (frequently marked by the upregulation of the cyclin-dependent kinase inhibitor *p16*^{Ink4a}, hereafter p16),[3,4] acquire a pro-inflammatory senescence-associated secretory phenotype (SASP),[5–8] exhibit macromolecular damage, and have metabolic deregulation.[9] Cells with features of senescence accumulate with age at sites of age-related pathology and are thought to promote tissue dysfunction through their loss of original function and acquisition of the pro-inflammatory SASP.[10,11] Therapeutically speaking, senescent cells offer a potential broad-spectrum target for the treatment of many age-related diseases. One such group of diseases where cellular senescence has been previously implicated is tauopathies.[12–14] Tauopathies are neurodegenerative diseases characterized by the deposition and hyperphosphorylation of the microtubule-associated protein tau (encoded by the *MAPT* gene) and include supranuclear palsy, Pick's disease, frontotemporal dementias, and Alzheimer's disease (AD).[15] Unfortunately, there are no curative therapies for these debilitating conditions.

AD is the most common form of dementia in humans, accounting for 60%–80% of all cases.[16,17] The effects of senescent cells, particularly p16-postive senescent cells, on AD progression are of ever-increasing interest. Increased p16 expression in neurons of patients with AD has been reported on for decades.[18,19] More recently, studies have shown that other brain cell types, particularly glial cells, also exhibit increased p16 expression in patients with AD.[20–22] For this reason, understanding the specific contribution of p16-dependent senescence to AD, and more broadly to tau-based pathology, could offer important mechanistic insight into senescence as a therapeutic target in neurodegenerative disease.

To study the role of p16-dependent senescence in tauopathy, we utilized *PS19* (*MAPT*^{P301S}) transgenic mice. These mice

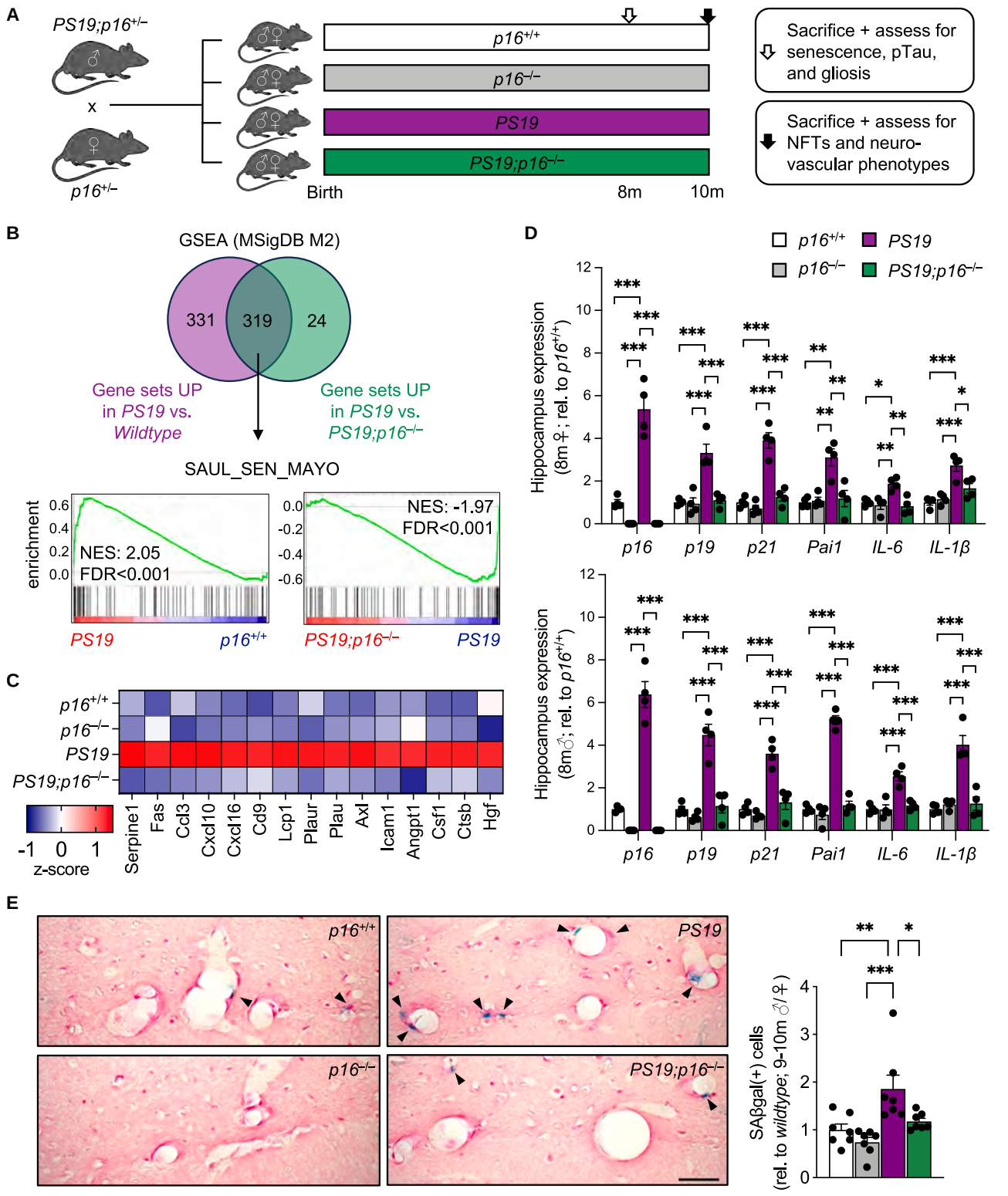

Figure 1. Genetic knockout of p16 attenuates senescence signatures in *PS19* mice

(A) Breeding scheme and experimental overview.

(B) Gene set enrichment analysis (GSEA) from bulk RNA-seq of 8-month-old female hippocampus in *PS19* mice, relative to both wild-type ($p16^{+/+}$) and *PS19;* $p16^{-/-}$ mice with normalized enrichment score (NES) and false discovery rate (FDR) indicated for the SenMayo gene set.

(legend continued on next page)

Table 1. GSEA of non-canonical p16 functions in 8-month-old *PS19*;*p16*$^{-/-}$ vs. *PS19* female mice

Predicted impact of *p16* deletion based on non-canonical function of p16	GSEA—gene set	NES	FDR q value
Increased MTORC1 activity	hallmark of MTORC1	−0.9074463	0.8595419
Increased NF-κB signaling	hallmark tumor necrosis factor alpha (TNF-α) signaling via NF-κB	−1.9607358	0.000212
Increased ROS	hallmark ROS pathway	−1.4168371	0.8595419
Increased mitochondrial biogenesis	Biocarta mitochondria pathway	−0.9991097	0.54
Increased JNK signaling	Han JNK signaling up	−1.359711	0.20650406
Increased translation	Reactome translation	−0.2538797	1
Decreased microRNA-146b-5p expression	MIR-146A-5P MIR-146B-5P	−1.395227	0.01235955

overexpress a mutant form of the human tau protein that is prone to hyperphosphorylation and aggregation into neurofibrillary tangles (NFTs),[23] which are molecularly analogous to those observed in human tauopathies. Overexpression of mutant tau is driven by the mouse prion protein promoter and primarily affects neurons of the central nervous system. Integration of the *PS19* transgene does result in a 249-kb deletion on chromosome 3, but this deletion affects no known reference genes.[24] *PS19* mice exhibit reactive gliosis, neurodegeneration, and cognitive decline beginning by 8 months of age.[12,23] Previously, we have shown that senescent glial cells accumulate in both the hippocampus and cortex of *PS19* mice with advancing disease, and chronic clearance of senescent cells by both genetic killing mechanisms and pharmacological intervention prevents tau-dependent disease.[12] Here, we investigate the role of p16-dependent maintenance of cellular senescence in tauopathy by knocking out this important cell-cycle regulator in *PS19* mice. We then implicate p16-expressing endothelial cells and microglia as specific drivers of tau-dependent neurodegenerative disease.

RESULTS

Genetic knockout of p16 attenuates senescence signatures in *PS19* mice

We crossed *PS19* mice onto a p16 null genetic background (Figure 1A) and evaluated these animals for tau-dependent disease. We first assessed how knockout of p16 impacted the acquisition of senescence-associated (SA) gene expression in the hippocampus of *PS19* mice, using bulk RNA sequencing (RNA-seq) (Figures S1A–S1D). Pathology in *PS19* mice typically initiates in the hippocampus, the neuron-dense brain region, important in memory and learning, then migrates outward to the cortex as disease progresses. Query of all curated gene sets in the Molecular Signatures Database (MSigDB M2) revealed a total of 650 gene sets enriched in *PS19* females, compared with wild-type (*p16*$^{+/+}$) littermates. Of these gene sets, 319 were also enriched in *PS19* mice relative to *PS19* mice lacking p16, which included the SenMayo gene set (Figures 1B and 1C). The SenMayo gene set has recently been defined and used to identify high senescent cell burden in multiple contexts.[25] Upregulated expression of leading-edge genes from the SenMayo gene set in *PS19* mice is prevented by knocking out p16, suggesting that the senescence burden in *PS19* mice depends on p16 expression (Figure 1C). We further validated this finding using quantitative reverse-transcription PCR (RT-qPCR) to determine the relative expression levels of a selected panel of SA genes in the hippocampus and cortex of an independent cohort of mice (Figures 1D and S1E). In agreement with our bulk RNA-seq experiments, *PS19* mice demonstrated increased expression of a variety of senescence indicators, including genes associated with cell-cycle arrest (*p16*, *p19*, and *p21*) as well as genes commonly associated with the SASP (*Pai1*, *Il-6*, *Il-1β*) relative to wild-type littermates. In the absence of p16, *PS19* mice demonstrated significantly lower expression levels of these SA genes in both female and male mice (Figures 1D and S1E). An additional feature of senescent cells is the acquisition of SA β-galactosidase (SA-β-gal) activity, indicative of increased lysosomal hydrolysis, that can be observed as blue cells after staining *in situ* tissue sections.[26] We found that *PS19* mice had more SA-β-gal(+) cells in the hippocampus, relative to both wild-type and *PS19* mice that are deficient for p16 (Figure 1E). Altogether, these results suggest that genetic ablation of p16 is sufficient to attenuate senescent cell accumulation in *PS19* mice. We found no evidence by gene set enrichment analysis (GSEA) to suggest that p16 deletion in *PS19* mice was affecting pathways related to non-canonical roles of p16 such as mechanistic target of rapamycin complex 1 (MTORC1) activation, nuclear factor κB (NF-κB) activation, increased reactive oxygen species (ROS), increased mitochondrial biogenesis, increased c-Jun N-terminal kinase (JNK) signaling, or increased translation (Table 1).[27,28] Knockout of p16 in *PS19* mice did result in alterations to known p16-stimulating tumor suppressive microRNAs, but there was no notable tumorigenesis in our experimental cohorts of mice, which were sacrificed between 8 and 12 months of age.

(C) Heatmap depicting average expression of leading-edge genes that are differentially expressed (padj < 0.05) from the SenMayo gene set. $N = 4$ mice per genotype.

(D) RT-qPCR analysis of SA gene expression in the hippocampus of 8-month-old wild-type and *PS19* female (top) and male (bottom) mice.

(E) Representative images (left) and quantification (right) of SA-β-gal activity (black arrows) in the hippocampus of 8-month-old female and male mice. Scale bar, 40 μm. Data points represent average expression per mouse with group mean ± SEM also indicated. $^{*}p < 0.05$, $^{**}p < 0.01$, $^{***}p < 0.001$ (one-way ANOVA with Tukey's multiple comparisons test).

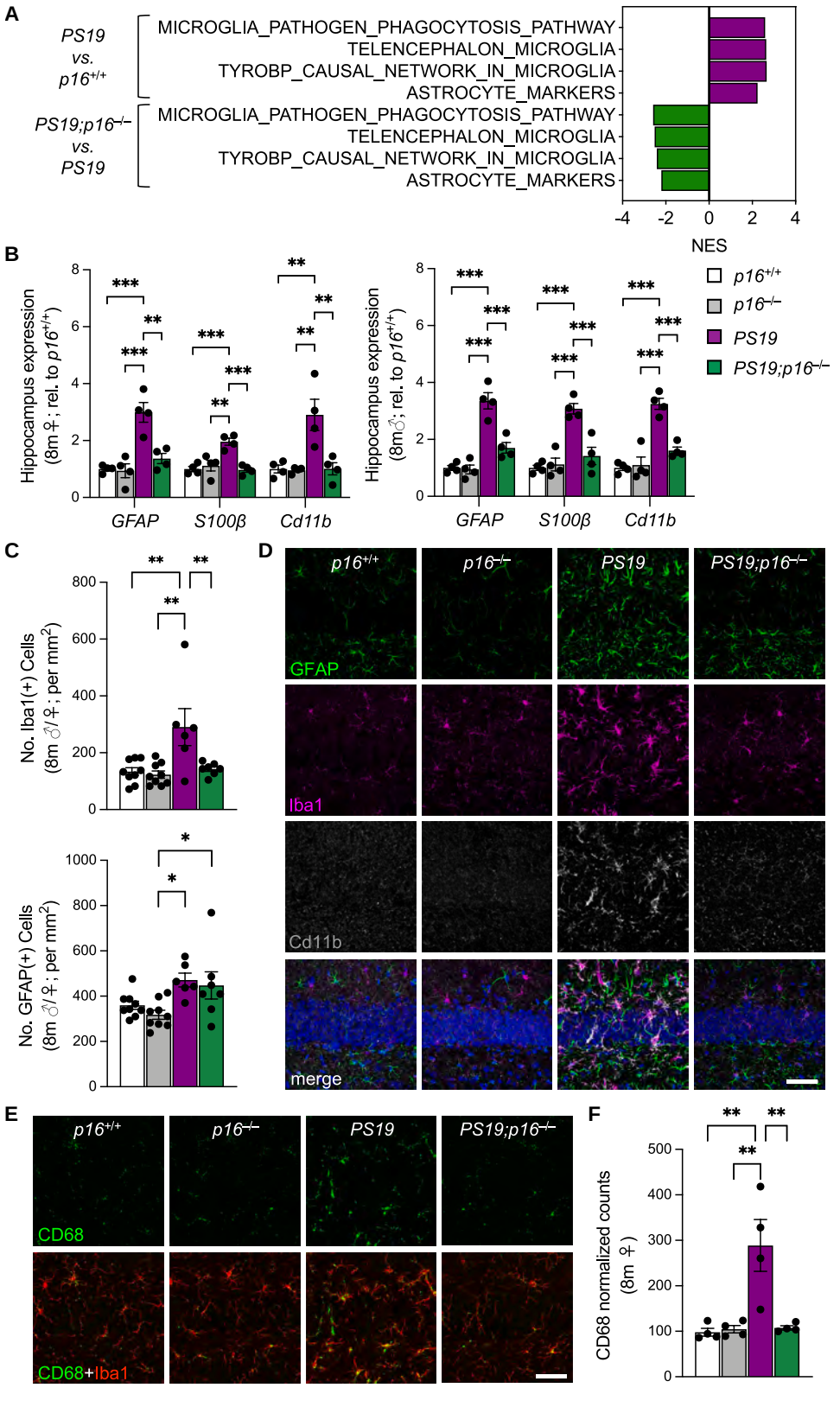

(legend on next page)

Neuroinflammation in *PS19* mice depends on p16 expression

We returned to our bulk RNA-seq dataset and performed a broader analysis of differentially expressed genes (DEGs; $\log_2$ fold change [FC] > 1, *p*adj < 0.05) that were upregulated in *PS19* mice, relative to both wild-type mice and *PS19;p16*$^{-/-}$ mice (Figure S1B). Gene Ontology analysis of these 69 DEGs returned terms that were most abundantly associated with the immune system (Figure S1B). DEGs in these terms were related to many aspects of the immune system, including pathogen response, natural killer cell signaling, interferon response, Toll-like receptor signaling, complement activation, and innate immunity (Figure S1C). Given these data, we next wanted to further explore the impact of p16 deletion on neuroinflammation in the brains of *PS19* mice.

Chronic neuroinflammation in the form of astrocytic reactivity and microglial activation, commonly referred to as "gliosis," is highly associated with neurodegenerative disease.[23,29,30] Prolonged signaling through these states is thought to promote neuronal dysfunction and cell death.[31] To first probe for neuroinflammation in *PS19* mice, we queried our bulk RNA-seq dataset for astrocytic- and microglial-specific gene sets that were enriched in *PS19* mice. We found three microglial gene sets and one astrocytic gene set that were enriched in *PS19* mice relative to both wild-type and *PS19* mice lacking p16 (Figures 2A and S2A). We then measured the expression of genes specific for activated astrocytes (glial fibrillary associated protein or GFAP, S100β) and microglia (Cd11b) by RT-qPCR in the hippocampus and cortex of an independent cohort of 8-month-old mice. We found an induction of these markers in *PS19* mice, which was attenuated with knockout of p16 (Figures 2B and S2B). To corroborate these changes, we performed immunofluorescence staining for reactive astrocytes (GFAP) and activated microglia (Cd11b and Iba1). *PS19* mice exhibited an increased number of Iba1(+) cells in the hippocampus, which was prevented with loss of p16 (Figures 2C and 2D). The number of GFAP(+) cells in *PS19* mice was not significantly different from wild-type or *PS19* mice deficient for p16 (Figure 2C). However, astrocytes in *PS19* mice showed morphological signs of activation, such as increased GFAP staining and increased soma size, which were prevented with genetic ablation of p16 (Figures 2D and S2C). Given that the "microglia pathogen phagocytosis pathway" was the most negatively enriched microglial-specific Gene Ontology term with knockout of p16 in *PS19* mice (Figure 2A), we performed immunofluorescence staining for CD68, a marker of actively phagocytosing microglia.[32] *PS19* mice exhibited increased CD68 staining in the dentate gyrus, compared with wild-type mice, which was prevented with genetic ablation of p16 (Figure 2E). Further exploration within our bulk RNA-seq dataset also revealed upregulation of CD68 and several other phagocytosis-related genes at the transcript level in *PS19* mice, relative to both wild-type and *PS19;p16*$^{-/-}$ mice (Figures 2F and S1D). Together, these results indicate that gliosis in *PS19* mice is driven, at least in part, through p16-expressing cells.

p16 promotes accumulation of pathological tau and neurodegeneration in *PS19*

Given the impacts of p16 loss in *PS19* mice on both senescence and neuroinflammation, we next assessed for impacts on tau pathology. Importantly, genetic ablation of p16 does not impact the amount of total transgenic tau that is produced in *PS19* mice (Figures 3A, 3B, S3A, and S3B). Loss of p16 does however prevent the accumulation of phosphorylated tau (pTAU) in *PS19* mice (Figures 3C, S3C, and S3D). The hyperphosphorylation of tau is a critical step in the progression of neurodegenerative disease.[33] As neurodegeneration progresses in *PS19* mice, pTAU progresses from dim, intra-neuronal staining to bright, intra-neuronal staining and eventually to bright, extracellular puncta as neurons die and leave behind pTAU aggregates in the extracellular space (Figures 3D and S3E). A similar progression of pTAU staining has been previously described in humans with AD.[34] We found that genetic ablation of p16 limits pTAU progression in *PS19* mice (Figure 3E). As tau becomes hyperphosphorylated, it aggregates into the pathogenic, sarkosyl-insoluble NFTs that are hallmarks of tauopathies.[33] To probe for these particularly pathogenic pTAU aggregates, we incubated brain lysates in sarkosyl and performed western blotting analyses for total tau and pTAU in sarkosyl- soluble and insoluble fractions, as we have done previously.[12] In the soluble fraction, knockout of p16 had no impact on total or pTAU levels (Figures 3F and 3G). In contrast, we observed less pTAU in the insoluble fraction in *PS19* mice lacking p16, supportive of p16 driving the formation of pathogenic NFTs (Figures 3F and 3G). To further support this, we treated brain sections with thioflavinS to visualize protein aggregates (Figure 3H). *PS19* mice exhibit many such aggregates in the granular cell layer of the dentate gyrus, a neuronal-rich area of the hippocampus, which were fewer in the absence of p16 (Figure 3H). Collectively, these data demonstrate that p16 expression exacerbates the conversion of tau into phosphorylated and pathogenic species.

Knockout of p16 prevents neurodegeneration and cognitive decline in *PS19* mice

As tau pathology progresses, *PS19* mice exhibit progressive neurodegeneration. This can be seen overtly as a hindlimb-clasping phenotype (Figure 4A). Genetic ablation of p16 attenuates this

Figure 2. Neuroinflammation in *PS19* mice depends on p16 expression

(A) Microglial- and astrocytic-related gene sets that are enriched (false discovery rate [FDR] < 0.25) in hippocampus of 8-month-old female *PS19* mice, compared with both wild-type (*p16*$^{+/+}$) and *PS19;p16*$^{-/-}$ females.

(B) RT-qPCR analysis of microglial and astrocytic reactivity markers in the hippocampus of 8-month-old female (left) and male (right) mice.

(C) Iba1(+) and GFAP(+) cell counts from immunofluorescence images of the dentate gyrus of 8-month-old female and male mice.

(D) Representative immunofluorescence staining of the dentate gyrus for nuclei (DAPI, blue), reactive astrocytes (GFAP, green), microglia (iba1, magenta), and activated microglia (cd11b, white) in 8-month-old female and male mice.

(E) Representative immunofluorescence images of the dentate gyrus for phagocytic (CD68, green) microglia (iba1, red) in 8-month-old female mice.

(F) Normalized CD68 counts from bulk RNA-seq of hippocampus from 8-month-old female mice. Scale bar, 50 μm. Data points represent averages per mouse with group mean ± SEM also indicated. **p* < 0.05, ***p* < 0.01, ****p* < 0.001 (one-way ANOVA with Tukey's multiple comparisons test).

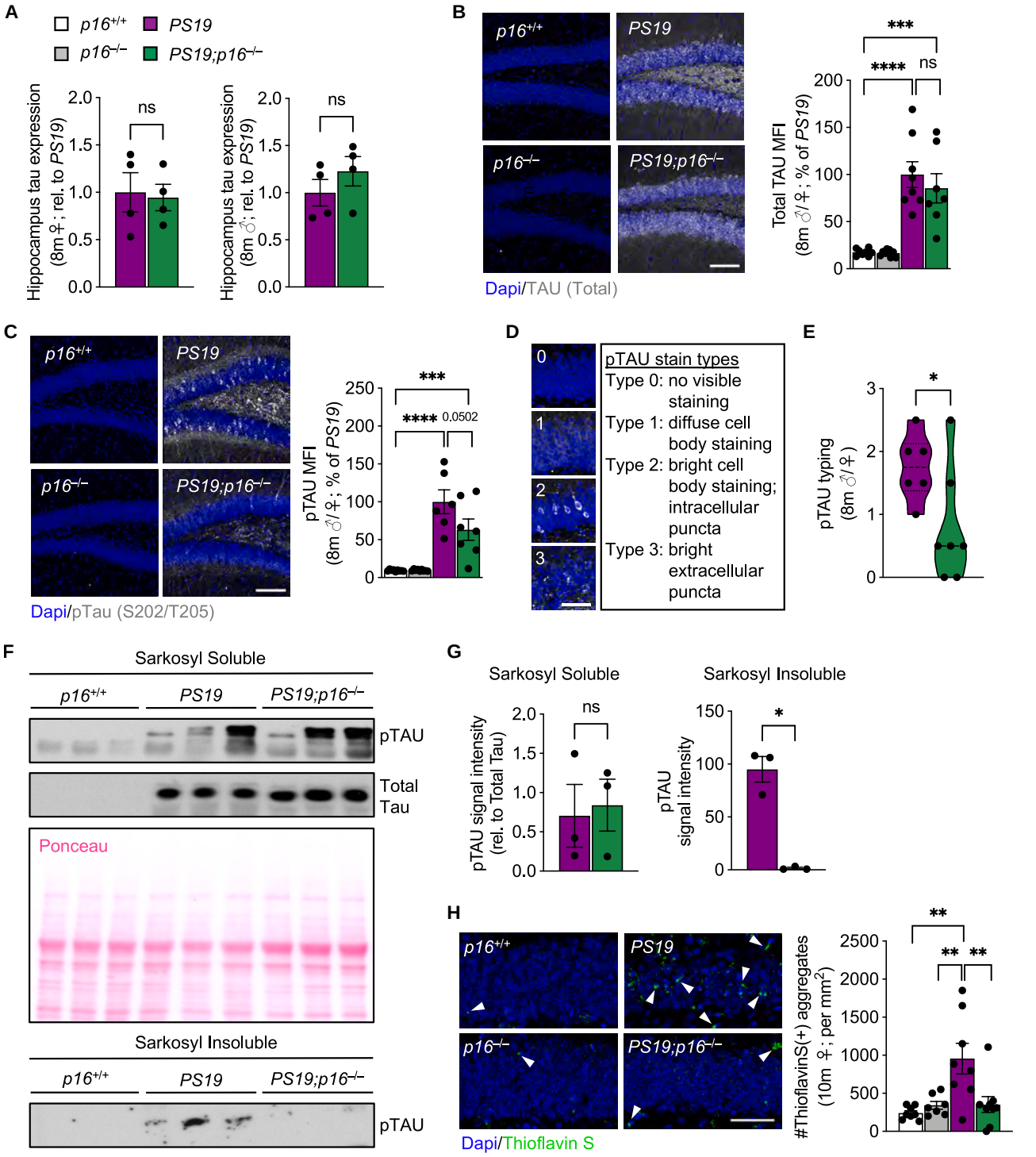

Figure 3. p16 promotes accumulation of pathological tau and neurodegeneration in *PS19* mice

(A) RT-qPCR analysis of total human tau expression in the hippocampus (right) of 8-month-old female (left) and male (right) mice.

(B) Representative immunofluorescence images (left) of nuclei (DAPI, blue) and total tau (white) and mean fluorescence intensity quantification (right) in the dentate gyrus of 8-month-old female and male mice.

(C) Representative immunofluorescence images (left) of nuclei (DAPI, blue) and phosphorylated tau (pTAU) (AT8, white) and mean fluorescence intensity quantification (right) in the dentate gyrus of 8-month-old female and male mice.

(D) pTAU stain typing guidelines.

(legend continued on next page)

hindlimb-clasping phenotype in *PS19* mice (Figure 4B). As neurodegeneration progresses, *PS19* mice also exhibit lower total body weight and general well-being as assessed by the nest building test, independent of p16 status (Figures S3F and S3G). To histologically assess for the impacts of p16 expression on neurodegeneration in the hippocampus, we performed Nissl staining to observe the thickness of the neuronal-rich granular cell layer of the dentate gyrus in *PS19* mice. We found that *PS19* mice had thinner granular cell layers than wild-type littermates by 10 months of age (Figure 4C). Additionally, *PS19* mice deficient for p16 had a thicker granular cell layer than *PS19* mice with intact p16 (Figure 4C). If *PS19* mice are allowed to age to 12 months, extensive neurodegeneration throughout the brain is reflected in total brain mass loss (Figure 4D). This is also attenuated with genetic ablation of p16 (Figure 4D).

PS19 mice exhibit cognitive decline in the form of memory and learning deficits.[35] We performed a battery of behavioral tests in our cohorts to assess for this. In the cued fear conditioning (CFC) test, mice were given a foot shock after a light and tone stimulus 24 h prior to testing. During testing, a mouse's capacity for associative learning was measured as fear-induced time spent freezing when the light and tone stimulus was present (Figure 4E). In this way, *PS19* mice showed a deficit in associative learning, compared with wild-type littermates, which was prevented with genetic ablation of p16 (Figure 4F). We also assessed for spatial working memory using the Y-maze where mice with intact spatial working memory and motivation are expected to spontaneously alternate through the three arms of the maze (Figure 4G). *PS19* mice exhibit a working spatial memory deficit, compared with wild-type littermates, which is attenuated with genetic ablation of p16 (Figure 4H). This protection is not due to differences in exploratory behavior as shown by similar total alternations made across genotypes during testing (Figure 4I). Finally, we also assessed for path integration ability in younger mice via the L-maze test. Others have shown that humans at risk for AD exhibit deficits in this type of spatial learning decades before exhibiting any clinical symptoms and that this deficit is attributed to brain volume loss specifically in the entorhinal cortex.[36] In the L-maze test, mice are trained to travel in an L shape from a start box to an escape hole. During testing, the maze is removed from the table and the mouse's ability to travel directly to the escape hole is measured as a low angular error (Figure 4J). *PS19* males exhibit a deficit in path integration, compared with wild-type littermates, months before histological changes can be seen in their brains (Figure 4K). This deficit was not significantly attenuated with knockout of p16. Interestingly, this deficit in path integration is not seen in female *PS19* mice, likely due to a higher average angular error made by wild-type females (Figure S3H). Altogether, these results suggest that p16 expression is critical for the neurodegeneration and some aspects of cognitive decline seen in *PS19* mice.

Altered neurovascular phenotypes are dependent on p16 expression in *PS19* mice

Another feature present in AD is the breakdown of the blood-brain barrier (BBB).[37] The primary BBB is composed of tight junctional complexes between the endothelial cells that make up blood vessel walls. This primary BBB is ensheathed by vascular mural cells—called pericytes—and astrocytic endfeet, which both regulate endothelial tight junctions.[38] Together, these cells communicate with neurons to form the neurovascular unit (NVU) and to maintain brain homeostasis via regulation of molecular transport and neurovascular coupling. Given our previous demonstration of astrocytic senescence in *PS19* mice[12] and the role of astrocytes in BBB maintenance,[39] we decided to investigate BBB organization and function in *PS19* mice. We first queried for endothelial-specific gene sets in our bulk RNA-seq dataset and found three such gene sets—apical surface, apical junction, and angiogenesis—that were enriched in *PS19* females, compared with both wild-type and *PS19* females deficient for p16 (Figures 5A and S4A). We also observed extravasation of the blood product, albumin, into the brain parenchyma and uptake into GFAP(+) cells in *PS19* mice, which correlated with pTAU burden (Figures 5B and S4C). As albumin is typically restricted to the periphery, its presence in GFAP(+) cells suggests a functional breakdown of the BBB in *PS19* mice.[40] To characterize any neurovascular dysfunction that might underlie such a BBB breakdown, we investigated whether any other members of the NVU were markedly changed in *PS19* mice. We noted no consistent changes in pericytes by immunofluorescence staining for CD13 (Figure S4B). However, *PS19* mice did exhibit a dilation and an increased number of hippocampal blood vessels (Figures 5C and 5D). We also observed that aquaporin-4 (AQP4), a key component of astrocytic endfeet, was depolarized from vessels in *PS19* mice (Figures 5C and 5D). This depolarization of AQP4 correlated with pTAU burden in *PS19* mice (Figure S4D). Unexpectedly, we also observed a disorganization of the endothelial cell extracellular matrix (ECM), as visualized by increased isolectin GS-IB4 binding outside of the vessel lumen (Figure 5E). Furthermore, while astrocytic endfoot depolarization and disorganized endothelial ECM were most prominent in the dentate gyrus of *PS19* mice, these neurovascular abnormalities were observable throughout brain regions along the perforant pathway (Figure S5), the primary route of neuronal projection from the entorhinal cortex to the hippocampus. The perforant pathway is also a major site of tau pathology and neurodegeneration in humans with

(E) pTAU typing results in *PS19* mice and *PS19;p16*$^{-/-}$ mice.
(F) Western blot for pTAU (AT8) and total tau in sarkosyl soluble (top) and sarkosyl insoluble (bottom) lysates from the cortex and hippocampus of 10-month-old female mice. Ponceau S was used to compare loading.
(G) Western blot quantification of pTAU in sarkosyl soluble (left) and sarkosyl insoluble (right) lysates.
(H) ThioflavinS staining (left, white arrows) and quantification of thioflavinS+ aggregates (right) in the dentate gyrus of 10-month-old female mice. Scale bars, 100 μm in (B) and (C) and 50 μm in (D) and (H). Data points represent averages per mouse with group mean ± SEM also indicated. $^{*}p < 0.05$, $^{**}p < 0.01$, $^{***}p < 0.001$, $^{****}p < 0.0001$ as determined by (B, C, and H) one-way ANOVA with Tukey's multiple comparisons test or (A, E, and G) unpaired two-sided t tests with Welch's correction.

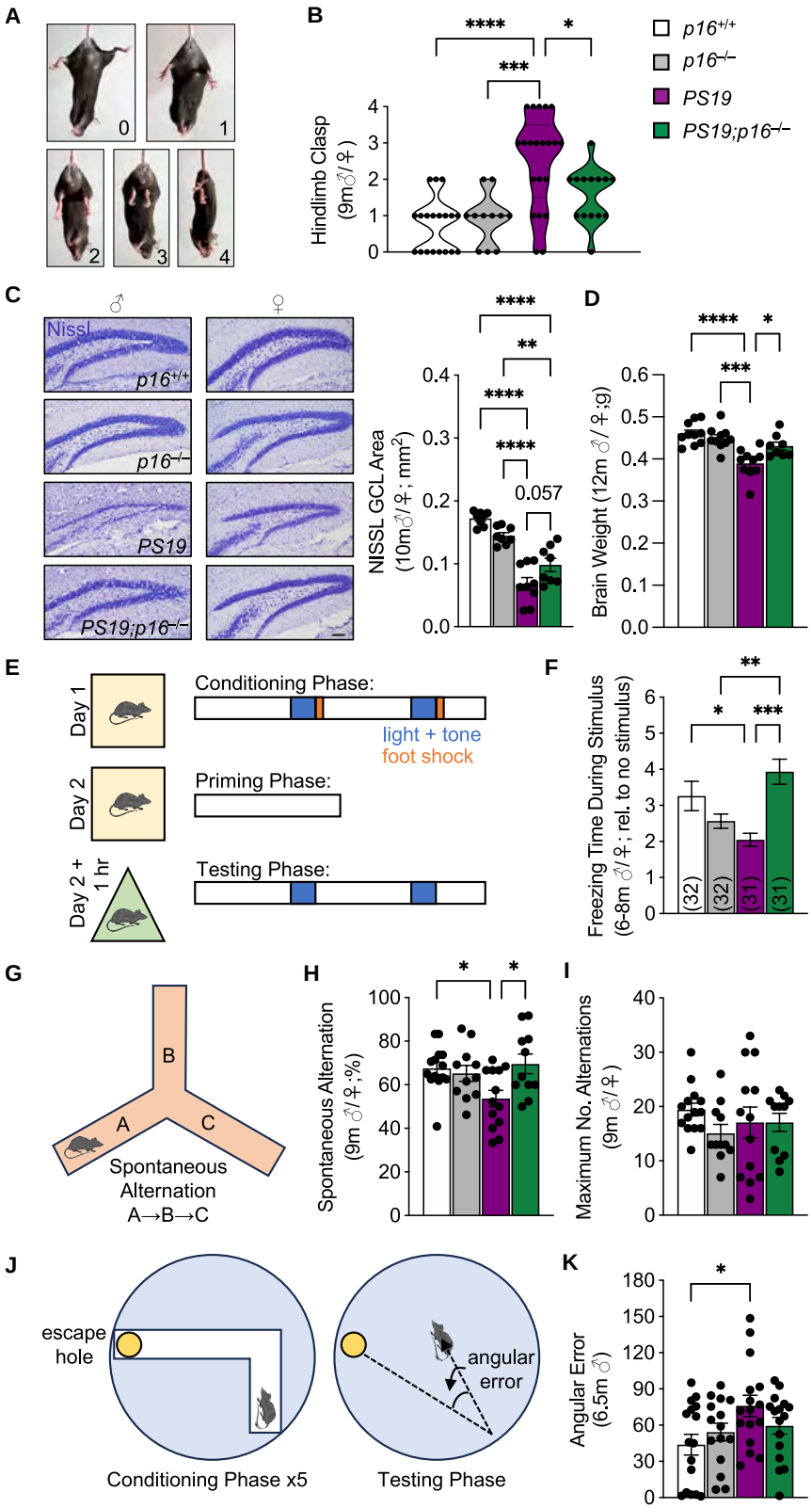

Figure 4. Knockout of p16 prevents neurodegeneration and cognitive decline in *PS19* mice

(A) Representative images of hindlimb-clasping scoring criteria in *PS19* mice.

(B) Hindlimb-clasping scores for 9-month-old female and male mice.

(C) Representative Nissl staining images (left) and granular cell layer (GCL) area measurement (right) of the dentate gyrus of 10-month-old female and male mice.

(D) Whole-brain weights of 12-month-old female and male mice.

(E) Schematic overview of cued-fear conditioning (CFC) experiment for assessment of fear-based memory formation in *PS19* mice.

(F) Freezing time FC when presented with the conditioned stimulus during the testing phase of the CFC assessment of 6- to 8-month-old female and male mice. $N = 31–32$ mice per group.

(G–I) (G) Schematic overview of Y-maze experiment for assessment of spatial working memory. Percentage of spontaneous alteration (H) and maximum alternations (I) in Y-maze assessment of 9-month-old female and male mice.

(J) Schematic overview of L-maze experiment for assessment of path integration ability.

(K) Angular error in 6.5-month-old male mice during the testing phase of the L-maze assessment. Scale bar, 100 μm. Data points represent averages per mouse with group mean ± SEM also indicated.

$^{*}p < 0.05$, $^{**}p < 0.01$, $^{***}p < 0.001$, $^{****}p < 0.0001$ determined by one-way ANOVA with Tukey's multiple comparisons test.

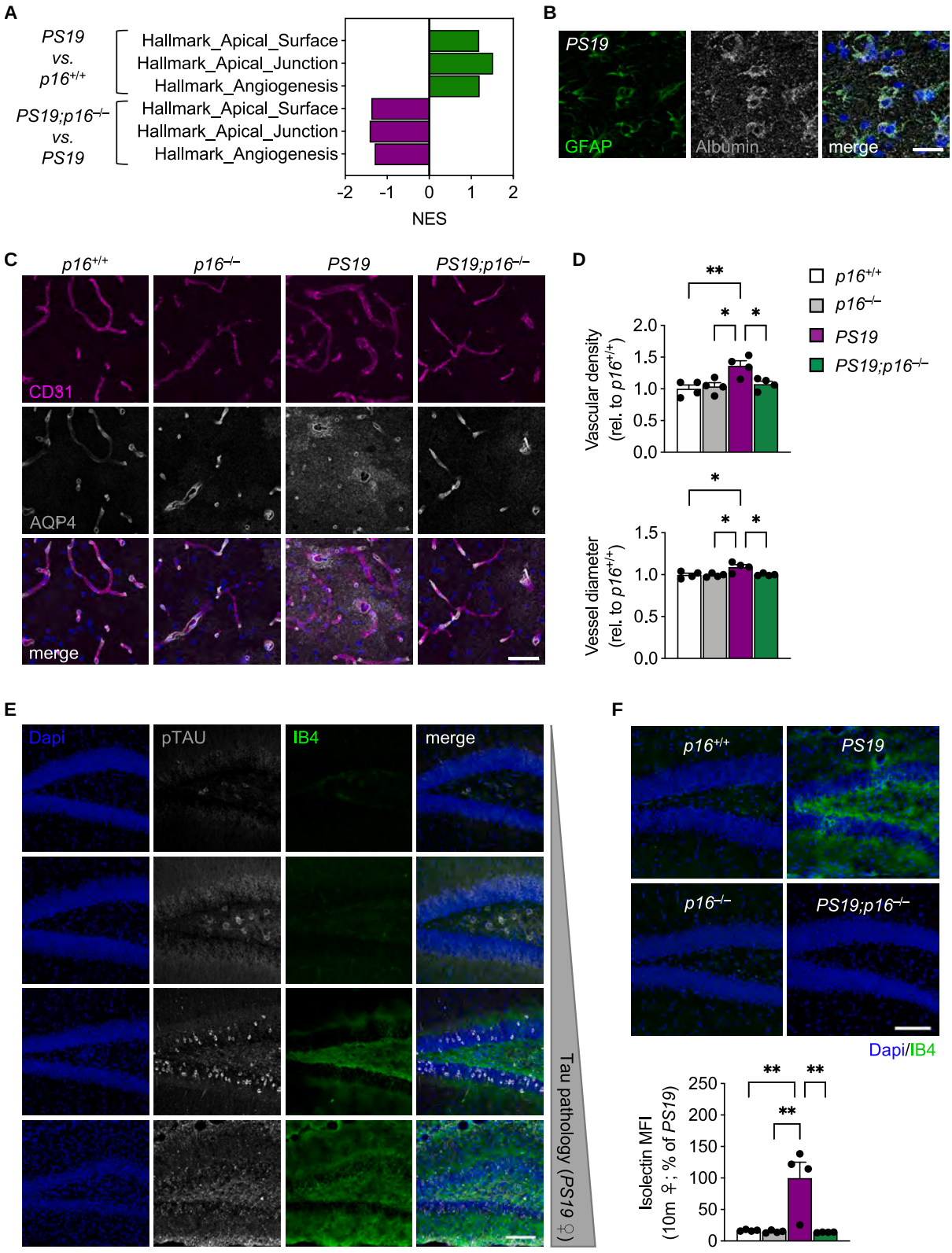

(legend on next page)

AD.[41,42] Genetic knockout of p16 prevented vessel dilation, astrocytic endfoot depolarization, and endothelial cell ECM disorganization (Figures 5C, 5D, 5F, and S5). These results indicate that p16 plays an essential role in the development of neurovascular abnormalities seen in *PS19* mice.

Selective knockout of p16 in Tie2(+) endothelial cells and microglia attenuates aspects of tau-dependent pathology in *PS19* mice

We next sought to understand which cell types might be involved in p16-dependent tau pathology. Originally, we observed SA-β-gal positivity in *PS19* brain cells that appeared to be vessel-associated (Figure 1E). Previous work has also implicated senescent microglia in *PS19* mice.[12,43] Given this information, we utilized *Tie2^{cre}* and *p16$^{fl/fl}$* mice to selectively knockout p16 in Tie2(+) endothelial cells and microglia in *PS19* mice (Figure 6A). We confirmed cre recombinase activity in our cell types of interest, using the Ai14 reporter mouse line, which contains a lox-stop-lox cassette upstream of a tomato sequence; cre-mediated excision of the stop cassette results in production of tomato and can be visualized with fluorescence microscopy. Indeed, we observed tomato positivity, a proxy of cre recombinase activity, in Ly6C(+) endothelial cells and Iba1(+) microglia in brains of *Tie2^{cre};Ai14* mice (Figure 6B).

To first assess for the impacts of p16 deletion in Tie2(+) cells on tau pathology, we performed immunofluorescence staining of brain sections for pTAU in *PS19;p16$^{fl/fl}$* mice with and without *Tie2^{cre}*. We observed a partial prevention of tau phosphorylation in *PS19* mice lacking endothelial- and microglial-p16 expression (Figure 6C). We next assessed for other tau-dependent phenotypes including gliosis, vascular abnormalities, neurodegeneration, and cognitive decline. Knockout of p16 in Tie2(+) cells reduced some but not all aspects of gliosis (Figures 6D, S6A, and S6B). Notably, p16 deletion in Tie2(+) cells resulted in increased microglial ramification, a sign of increased microglial homeostasis (Figure 6D). We also observed less depolarization of astrocytic endfeet processes and decreased endothelial ECM deregulation with knockout of p16 in Tie2(+) cells (Figures 6E and 6F). Knockout of p16 in Tie2(+) cells also resulted in higher gross brain weights and increased Nissl staining in the neuron-rich granular cell layer of the dentate gyrus in the hippocampus (Figures 6G, 6H, and S6C). Finally, p16 deletion in Tie2(+) endothelial cells and microglia resulted in improved working spatial memory, as assessed by the Y-maze test (Figures 6I and S6D). Altogether, p16 expression, specifically in Tie2(+) microglia and endothelial cells, is required for most tau-dependent phenotypes in *PS19* mice.

DISCUSSION

Previous work has demonstrated that removal of senescent cells prevents tauopathy in mice. Our work further implicates senescent cells in the progression of neurodegenerative disease by showing that an intact p16-dependent cell-cycle arrest pathway is necessary for tau pathology. In this study, we demonstrated that genetic ablation of a singular key senescence mediator prevents senescent cell accumulation, gliosis, tau phosphorylation, neurodegeneration, and cognitive decline in *PS19* mice. Additionally, we demonstrated that *PS19* mice exhibit abnormal neurovascular phenotypes that correlate with the severity of tau pathology and that these abnormalities are attenuated with genetic ablation of p16. BBB disruption is a well-established feature of human AD; however, few studies have molecularly linked tau pathology and neurovascular abnormalities. The findings of this study suggest that an intact p16-dependent cell-cycle arrest pathway is necessary for tau-based neurovascular changes.

This study is limited by both the use of a tau-only mouse model of disease and by the use the of p16 deletion to mitigate senescent cell accumulation. In humans, AD is typically characterized by both aberrant tau pathology and aberrant amyloid pathology. Future studies are needed to interrogate the role of p16-expressing cells in models of amyloid-only pathology and in models of mixed amyloid and tau pathology. Another limitation is that utilizing p16 deletion as a tool to prevent the cell-cycle arrest that underlies senescent cell accumulation is an incomplete approach to senescence mitigation, as there are p16-independent mechanisms by which a cell can become growth arrested and enter a senescent state, namely, through p21 upregulation. Additionally, p16 has known tumor suppressor roles, and knockout of p16 leads to increased cancer frequency. However, in this study, mice were sacrificed and analyzed prior to 12 months of age and before any notable levels of tumorigenesis in p16-null mice. Because we believe it is the senescent cells themselves that promote tauopathy, rather than p16 expression alone, future studies should utilize more therapeutically viable and broad-spectrum approaches to mitigate senescent cell burden, such as senolytics and senomorphics. Indeed, several studies

Figure 5. Altered neurovascular phenotypes are dependent on p16 expression in *PS19* mice

(A) Endothelial cell-related gene sets enriched in the hippocampus of 8-month-old *PS19* female mice, relative to both wild-type (*p16$^{+/+}$*) and *PS19;p16$^{-/-}$* females.

(B) Representative immunofluorescence staining showing co-localization of extravasated blood protein (albumin, white) with astrocytes (GFAP, green) in *PS19* mice.

(C) Representative immunofluorescence staining of nuclei (DAPI, blue), endothelial cells (CD31, magenta), and astrocytic endfeet (AQP4, white) in the dentate gyrus of 10-month-old female mice.

(D) Average vascular density (top) and vessel diameter (bottom) in the dentate gyrus of 10-month-old female mice.

(E) Representative immunofluorescence staining of nuclei (DAPI, blue), pTAU (AT8, white), and endothelial ECM (GS-IB4, green) in female *PS19* mice in order of increasing tau pathology.

(F) Representative immunofluorescence images (top) of nuclei (DAPI, blue) and endothelial ECM (GS-IB4, green) and quantification (bottom) in 10-month-old female mice. Scale bars, 20 μm in (B), 50 μm in (C), and 100 μm in (E) and (F). Data points represent averages per mouse with group mean ± SEM. $^{*}p < 0.05$, $^{**}p < 0.01$, $^{***}p < 0.001$ (one-way ANOVA with Tukey's multiple comparisons test).

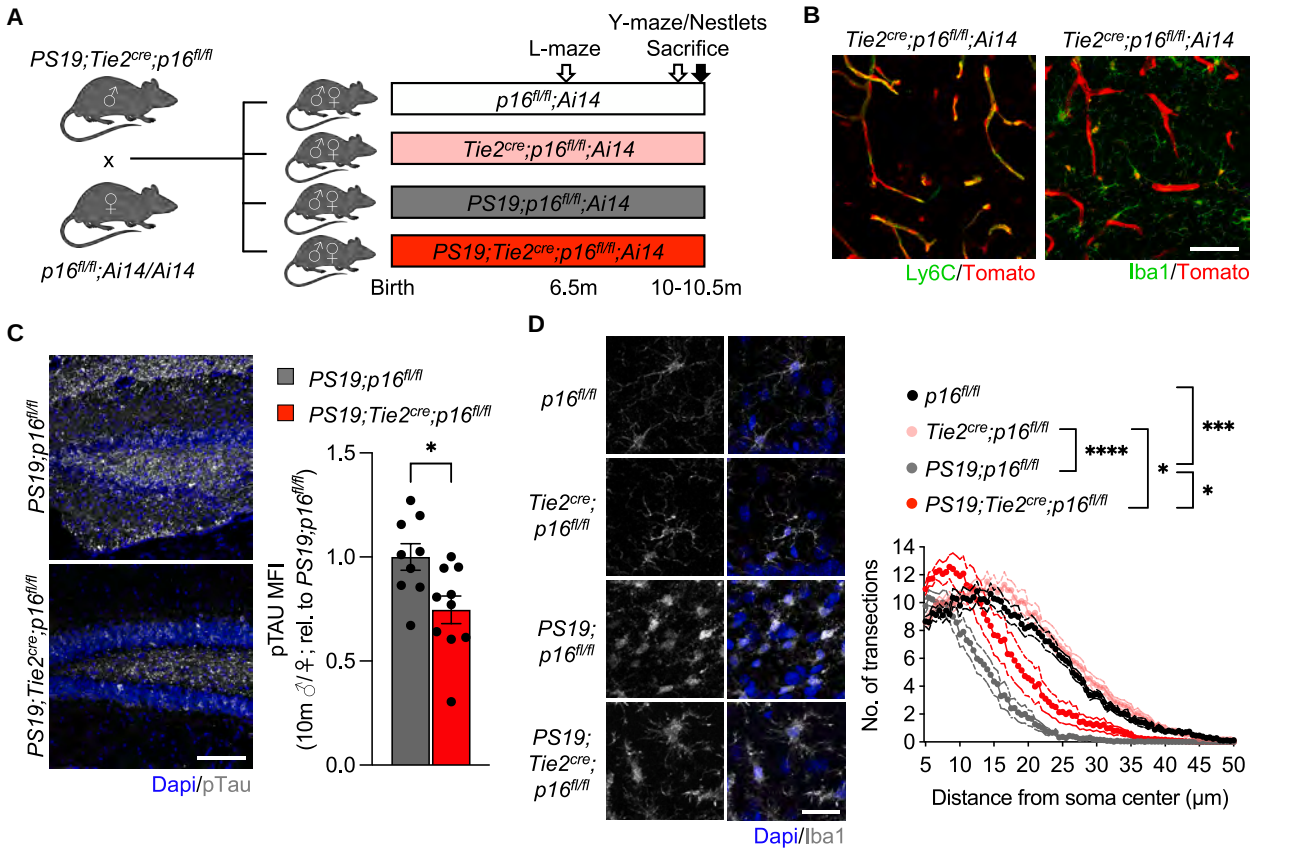

(legend on next page)

have targeted senescent cells in such a way and have shown attenuation of disease in various mouse models of AD.[12–14]

The cell-type specificity of senescence as it contributes to age-related diseases, like neurodegeneration, is of high interest currently. The heterogeneity and lack of reliable markers for senescent cells have made it challenging to identify the specific cell types becoming senescent in *in vivo* contexts. Here, microgliosis and phagocytosis are strongly attenuated with whole-body knockout of p16 in *PS19* mice. Previous studies have shown increased phagocytosis in microglia exposed to pTAU and that such alterations in phagocytosis can lead to signs of microglial senescence.[22,44,45] Previous work in *PS19* mice has also demonstrated that microglia can exhibit high expression of SA markers.[12,43] In this study, we showed SA-β-gal activity in cells closely associated with vessels, particularly those of the stratum lacunosum moleculare, which connects the entorhinal cortex and the hippocampus along the perforant pathway of learning and memory. Given the evidence for senescence in microglia and vessel-associated cells in *PS19* mice, the *Tie2^{cre}* system offered a unique opportunity to study the effects of p16 deletion in both endothelial cells and microglia. We showed that knockout of p16 in these cell types attenuated many of the same phenotypes that whole-body knockout of p16 does, albeit in moderation. Knockout of p16 in these cell types led to 25%–50% attenuation of disease depending on the phenotype. This partial attenuation of disease could be due to several factors including partial cre-mediated recombination in targeted cells, p16-independent mechanisms of senescence in endothelial cells and microglia, and/or the contribution of other senescent cell types to disease. Using a cell-type-specific senescence-targeting strategy in an *in vivo* model of tauopathy provides important evidence for endothelial and microglial senescence as drivers of disease. Future studies using a similar approach are needed to determine the contribution of other senescent cell types to tauopathy as well as to dissect how much of the disease modification in this study is due to endothelial vs. microglial senescence. Additional studies are needed to determine how p16 expression in specific cell types regulates the interplay between neurovascular changes and tauopathy to better understand how senescence contributes to neurodegenerative disease.

RESOURCE AVAILABILITY

Lead contact

Further information and requests for resources and reagents should be directed to and will be fulfilled by the lead contact, Darren Baker (baker.darren@mayo.edu).

Materials availability

This study did not generate new unique reagents.

Data and code availability

- RNA-seq data have been deposited at GEO at GEO: GSE294816 and are publicly available as of the date of publication.
- Original western blot images and microscopy data reported in this paper will be shared by the lead contact upon request.
- This paper does not report original code.
- Any additional information required to reanalyze the data reported in this paper is available from the lead contact upon request.

ACKNOWLEDGMENTS

We would like to thank T. Bussian for his valuable input during the initial stages of this project, K. Wininger and D.S. Choi for assistance with behavioral fear conditioning experiments, T. Thao and R. Fierro Velasco for genotyping and animal support, G. Su for guidance on working with p16 floxed mice, and the Mayo Clinic Genome Analysis Core for RT-qPCR instrumentation. Graphical abstract was generated using Biorender with permissions to S.I.G. (2025) https://BioRender.com/mc40fwf. This work was supported by the National Institutes of Health (R01AG053229 and R01AG068076), the Minnesota Partnership for Biotechnology and Medical Genomics (MNP #18.04), and the Glenn Foundation for Medical Research (all to D.J.B.).

AUTHOR CONTRIBUTIONS

S.I.G., C.F.M., and D.J.B. designed experiments and wrote the manuscript. K. B.J. performed western blotting experiments. C.F.M. performed cued-fear conditioning experiments. D.J.B. performed RT-qPCR experiments. S.I.G. performed all other experiments. All authors discussed results and edited the manuscript and figures. D.J.B. conceived, directed, and supervised all aspects of the study.

DECLARATION OF INTERESTS

D.J.B. has a potential financial interest related to this research. He is a co-inventor on patents held by Mayo Clinic and patent applications licensed to or

Figure 6. Selective knockout of p16 in Tie2(+) endothelial cells and microglia partially attenuates tau-dependent pathology *PS19* mice

(A) Breeding scheme and project overview for the selective knockout of *p16* in Tie2(+) cells in *PS19* mice.

(B) Representative images showing cre-mediated recombination of the Ai14 locus (tomato, red) in Ly6C(+) endothelial cells (left, green) and Iba1(+) microglia (right, green) in *Tie2^{cre}* mice.

(C) Representative immunofluorescence images (left) of nuclei (DAPI, blue) and pTAU (AT8, white) and mean fluorescence intensity quantification (right) in the dentate gyrus of 10-month-old female and male *PS19* mice with and without knockout of *p16* in Tie2(+) cells.

(D) Representative immunofluorescence images (left) of nuclei (DAPI, blue) and microglia (iba1, white) and sholl analysis of microglial ramification (right) in 10-month-old female and male mice.

(E) Representative immunofluorescence staining of nuclei (DAPI, blue), endothelial cells (Ly6C, green), and astrocytic endfeet (AQP4, white) in the dentate gyrus of 10-month-old mice female (top) and male (bottom) mice.

(F) Representative immunofluorescence images (left) of nuclei (DAPI, blue) and endothelial ECM (GS-IB4, green) and IB4 mean fluorescence intensity (right) in 10-month-old female and male mice.

(G) Whole-brain weights of 10-month-old female and male mice.

(H) Representative Nissl staining images (left) of the dentate gyrus of 10-month-old female (top) and male (bottom) mice.

(I) Percentage of spontaneous alteration in the Y-maze cognitive assessment of working spatial memory in 10-month-old *PS19* female and male mice. Scale bars, 50 μm in (B) and (E), 100 μm in (C) and (F), 25 μm in (D), and 200 μm in (H). Data points represent averages per mouse with group mean ± SEM also indicated. $^{*}p < 0.05$, $^{**}p < 0.01$, $^{***}p < 0.001$, $^{****}p < 0.0001$ as determined by (C) and (I) unpaired two-sided t test with Welch's correction, (D) two-way ANOVA with Tukey's multiple comparisons test, and (F and G) one-way ANOVA with Tukey's multiple comparisons test.

filed by Unity Biotechnology and is a Unity Biotechnology shareholder. Research in the Baker laboratory has been reviewed by the Mayo Clinic Conflict of Interest Review Board and is being conducted in compliance with Mayo Clinic Conflict of Interest policies.

STAR★METHODS

Detailed methods are provided in the online version of this paper and include the following:

- KEY RESOURCES TABLE
- EXPERIMENTAL MODEL
- METHOD DETAILS
  - Statistical analysis
  - Bulk RNA Sequencing
  - Quantitative PCR
  - Senescence-associated β-galactosidase Staining
  - Western blotting for soluble and sarkosyl insoluble proteins
  - Immunofluorescence
  - Nissl Staining
  - Hindlimb Clasping Scoring
  - Cued Fear Conditioning
  - Y-maze
  - L-maze
  - Nestlets
  - Vessel Diameter Measurement

SUPPLEMENTAL INFORMATION

Supplemental information can be found online at https://doi.org/10.1016/j.neuron.2025.04.020.

Received: July 8, 2024
Revised: November 15, 2024
Accepted: April 21, 2025
Published: May 16, 2025

REFERENCES

1. Flatt, T. (2012). A New Definition of Aging? Front. Genet. *3*, 148. https://doi.org/10.3389/fgene.2012.00148.
2. Di Micco, R., Krizhanovsky, V., Baker, D., and d'Adda di Fagagna, F. (2021). Cellular senescence in ageing: from mechanisms to therapeutic opportunities. Nat. Rev. Mol. Cell Biol. *22*, 75–95. https://doi.org/10.1038/s41580-020-00314-w.
3. Alcorta, D.A., Xiong, Y., Phelps, D., Hannon, G., Beach, D., and Barrett, J. C. (1996). Involvement of the cyclin-dependent kinase inhibitor p16 (INK4a) in replicative senescence of normal human fibroblasts. Proc. Natl. Acad. Sci. USA *93*, 13742–13747. https://doi.org/10.1073/pnas.93.24.13742.
4. Serrano, M., Hannon, G.J., and Beach, D. (1993). A new regulatory motif in cell-cycle control causing specific inhibition of cyclin D/CDK4. Nature *366*, 704–707. https://doi.org/10.1038/366704a0.
5. Acosta, J.C., Banito, A., Wuestefeld, T., Georgilis, A., Janich, P., Morton, J.P., Athineos, D., Kang, T.W., Lasitschka, F., Andrulis, M., et al. (2013). A complex secretory program orchestrated by the inflammasome controls paracrine senescence. Nat. Cell Biol. *15*, 978–990. https://doi.org/10.1038/ncb2784.
6. Coppé, J.P., Desprez, P.Y., Krtolica, A., and Campisi, J. (2010). The senescence-associated secretory phenotype: the dark side of tumor suppression. Annu. Rev. Pathol. *5*, 99–118. https://doi.org/10.1146/annurev-pathol-121808-102144.
7. Coppé, J.P., Patil, C.K., Rodier, F., Sun, Y., Muñoz, D.P., Goldstein, J., Nelson, P.S., Desprez, P.Y., and Campisi, J. (2008). Senescence-associated secretory phenotypes reveal cell-nonautonomous functions of oncogenic RAS and the p53 tumor suppressor. PLoS Biol. *6*, 2853–2868. https://doi.org/10.1371/journal.pbio.0060301.
8. Kuilman, T., Michaloglou, C., Vredeveld, L.C.W., Douma, S., van Doorn, R., Desmet, C.J., Aarden, L.A., Mooi, W.J., and Peeper, D.S. (2008). Oncogene-induced senescence relayed by an interleukin-dependent inflammatory network. Cell *133*, 1019–1031. https://doi.org/10.1016/j.cell.2008.03.039.
9. Gorgoulis, V., Adams, P.D., Alimonti, A., Bennett, D.C., Bischof, O., Bishop, C., Campisi, J., Collado, M., Evangelou, K., Ferbeyre, G., et al. (2019). Cellular Senescence: Defining a Path Forward. Cell *179*, 813–827. https://doi.org/10.1016/j.cell.2019.10.005.
10. Baker, D.J., Wijshake, T., Tchkonia, T., LeBrasseur, N.K., Childs, B.G., van de Sluis, B., Kirkland, J.L., and van Deursen, J.M. (2011). Clearance of p16Ink4a-positive senescent cells delays ageing-associated disorders. Nature *479*, 232–236. https://doi.org/10.1038/nature10600.
11. Baker, D.J., Childs, B.G., Durik, M., Wijers, M.E., Sieben, C.J., Zhong, J., Saltness, R.A., Jeganathan, K.B., Verzosa, G.C., Pezeshki, A., et al. (2016). Naturally occurring p16Ink4a-positive cells shorten healthy lifespan. Nature *530*, 184–189. https://doi.org/10.1038/nature16932.
12. Bussian, T.J., Aziz, A., Meyer, C.F., Swenson, B.L., van Deursen, J.M., and Baker, D.J. (2018). Clearance of senescent glial cells prevents tau-dependent pathology and cognitive decline. Nature *562*, 578–582. https://doi.org/10.1038/s41586-018-0543-y.
13. Musi, N., Valentine, J.M., Sickora, K.R., Baeuerle, E., Thompson, C.S., Shen, Q., and Orr, M.E. (2018). Tau protein aggregation is associated with cellular senescence in the brain. Aging Cell *17*, e12840. https://doi.org/10.1111/acel.12840.
14. Zhang, P., Kishimoto, Y., Grammatikakis, I., Gottimukkala, K., Cutler, R.G., Zhang, S., Abdelmohsen, K., Bohr, V.A., Misra Sen, J., Gorospe, M., et al. (2019). Senolytic therapy alleviates Aβ-associated oligodendrocyte progenitor cell senescence and cognitive deficits in an Alzheimer's disease model. Nat. Neurosci. *22*, 719–728. https://doi.org/10.1038/s41593-019-0372-9.
15. Spillantini, M.G., and Goedert, M. (2013). Tau pathology and neurodegeneration. Lancet Neurol. *12*, 609–622. https://doi.org/10.1016/S1474-4422(13)70090-5.
16. Kapasi, A., DeCarli, C., and Schneider, J.A. (2017). Impact of multiple pathologies on the threshold for clinically overt dementia. Acta Neuropathol. *134*, 171–186. https://doi.org/10.1007/s00401-017-1717-7.
17. Brenowitz, W.D., Hubbard, R.A., Keene, C.D., Hawes, S.E., Longstreth, W. T., Jr., Woltjer, R.L., and Kukull, W.A. (2017). Mixed neuropathologies and estimated rates of clinical progression in a large autopsy sample. Alzheimers Dement. *13*, 654–662. https://doi.org/10.1016/j.jalz.2016.09.015.
18. Arendt, T., Rödel, L., Gärtner, U., and Holzer, M. (1996). Expression of the cyclin-dependent kinase inhibitor p16 in Alzheimer's disease. Neuroreport *7*, 3047–3049. https://doi.org/10.1097/00001756-199611250-00050.
19. McShea, A., Harris, P.L., Webster, K.R., Wahl, A.F., and Smith, M.A. (1997). Abnormal expression of the cell cycle regulators P16 and CDK4 in Alzheimer's disease. Am. J. Pathol. *150*, 1933–1939.
20. Bhat, R., Crowe, E.P., Bitto, A., Moh, M., Katsetos, C.D., Garcia, F.U., Johnson, F.B., Trojanowski, J.Q., Sell, C., and Torres, C. (2012). Astrocyte senescence as a component of Alzheimer's disease. PLoS One *7*, e45069. https://doi.org/10.1371/journal.pone.0045069.
21. Hu, Y., Fryatt, G.L., Ghorbani, M., Obst, J., Menassa, D.A., Martin-Estebane, M., Muntslag, T.A.O., Olmos-Alonso, A., Guerrero-Carrasco, M., Thomas, D., et al. (2021). Replicative senescence dictates the emergence of disease-associated microglia and contributes to Aβ pathology. Cell Rep. *35*, 109228. https://doi.org/10.1016/j.celrep.2021.109228.
22. Gaikwad, S., Puangmalai, N., Bittar, A., Montalbano, M., Garcia, S., McAllen, S., Bhatt, N., Sonawane, M., SenGupta, U., and Kayed, R. (2021). Tau oligomer induced HMGB1 release contributes to cellular senescence and neuropathology linked to Alzheimer's disease and

frontotemporal dementia. Cell Rep. *36*, 109419. https://doi.org/10.1016/j.celrep.2021.109419.

23. Yoshiyama, Y., Higuchi, M., Zhang, B., Huang, S.M., Iwata, N., Saido, T.C., Maeda, J., Suhara, T., Trojanowski, J.Q., and Lee, V.M.Y. (2007). Synapse loss and microglial activation precede tangles in a P301S tauopathy mouse model. Neuron *53*, 337–351. https://doi.org/10.1016/j.neuron.2007.01.010.
24. Goodwin, L.O., Splinter, E., Davis, T.L., Urban, R., He, H., Braun, R.E., Chesler, E.J., Kumar, V., van Min, M., Ndukum, J., et al. (2019). Large-scale discovery of mouse transgenic integration sites reveals frequent structural variation and insertional mutagenesis. Genome Res. *29*, 494–505. https://doi.org/10.1101/gr.233866.117.
25. Saul, D., Kosinsky, R.L., Atkinson, E.J., Doolittle, M.L., Zhang, X., LeBrasseur, N.K., Pignolo, R.J., Robbins, P.D., Niedernhofer, L.J., Ikeno, Y., et al. (2022). A new gene set identifies senescent cells and predicts senescence-associated pathways across tissues. Nat. Commun. *13*, 4827. https://doi.org/10.1038/s41467-022-32552-1.
26. Dimri, G.P., Lee, X., Basile, G., Acosta, M., Scott, G., Roskelley, C., Medrano, E.E., Linskens, M., Rubelj, I., and Pereira-Smith, O. (1995). A biomarker that identifies senescent human cells in culture and in aging skin in vivo. Proc. Natl. Acad. Sci. USA *92*, 9363–9367. https://doi.org/10.1073/pnas.92.20.9363.
27. Al-Khalaf, H.H., Mohideen, P., Nallar, S.C., Kalvakolanu, D.V., and Aboussekhra, A. (2013). The cyclin-dependent kinase inhibitor p16INK4a physically interacts with transcription factor Sp1 and cyclin-dependent kinase 4 to transactivate microRNA-141 and microRNA-146b-5p spontaneously and in response to ultraviolet light-induced DNA damage. J. Biol. Chem. *288*, 35511–35525. https://doi.org/10.1074/jbc.M113.512640.
28. Buj, R., and Aird, K.M. (2019). p16: cycling off the beaten path. Mol. Cell. Oncol. *6*, e1677140. https://doi.org/10.1080/23723556.2019.1677140.
29. Bates, K.A., Fonte, J., Robertson, T.A., Martins, R.N., and Harvey, A.R. (2002). Chronic gliosis triggers Alzheimer's disease-like processing of amyloid precursor protein. Neuroscience *113*, 785–796. https://doi.org/10.1016/s0306-4522(02)00230-0.
30. Beach, T.G., Walker, R., and McGeer, E.G. (1989). Patterns of gliosis in Alzheimer's disease and aging cerebrum. Glia *2*, 420–436. https://doi.org/10.1002/glia.440020605.
31. Livne-Bar, I., Lam, S., Chan, D., Guo, X., Askar, I., Nahirnyj, A., Flanagan, J.G., and Sivak, J.M. (2016). Pharmacologic inhibition of reactive gliosis blocks TNF-α-mediated neuronal apoptosis. Cell Death Dis. *7*, e2386. https://doi.org/10.1038/cddis.2016.277.
32. Walker, D.G., and Lue, L.-F. (2015). Immune phenotypes of microglia in human neurodegenerative disease: challenges to detecting microglial polarization in human brains. Alzheimers Res. Ther. *7*, 56. https://doi.org/10.1186/s13195-015-0139-9.
33. Alonso, A.d.C., Grundke-Iqbal, I., and Iqbal, K. (1996). Alzheimer's disease hyperphosphorylated tau sequesters normal tau into tangles of filaments and disassembles microtubules. Nat. Med. *2*, 783–787. https://doi.org/10.1038/nm0796-783.
34. Moloney, C.M., Labuzan, S.A., Crook, J.E., Siddiqui, H., Castanedes-Casey, M., Lachner, C., Petersen, R.C., Duara, R., Graff-Radford, N.R., Dickson, D.W., et al. (2023). Phosphorylated tau sites that are elevated in Alzheimer's disease fluid biomarkers are visualized in early neurofibrillary tangle maturity levels in the post mortem brain. Alzheimers Dement. *19*, 1029–1040. https://doi.org/10.1002/alz.12749.
35. Takeuchi, H., Iba, M., Inoue, H., Higuchi, M., Takao, K., Tsukita, K., Karatsu, Y., Iwamoto, Y., Miyakawa, T., Suhara, T., et al. (2011). P301S mutant human tau transgenic mice manifest early symptoms of human tauopathies with dementia and altered sensorimotor gating. PLoS One *6*, e21050. https://doi.org/10.1371/journal.pone.0021050.
36. Bierbrauer, A., Kunz, L., Gomes, C.A., Luhmann, M., Deuker, L., Getzmann, S., Wascher, E., Gajewski, P.D., Hengstler, J.G., Fernandez-Alvarez, M., et al. (2020). Unmasking selective path integration deficits in Alzheimer's disease risk carriers. Sci. Adv. *6*, eaba1394. https://doi.org/10.1126/sciadv.aba1394.
37. Montagne, A., Barnes, S.R., Sweeney, M.D., Halliday, M.R., Sagare, A.P., Zhao, Z., Toga, A.W., Jacobs, R.E., Liu, C.Y., Amezcua, L., et al. (2015). Blood-brain barrier breakdown in the aging human hippocampus. Neuron *85*, 296–302. https://doi.org/10.1016/j.neuron.2014.12.032.
38. Daneman, R., and Prat, A. (2015). The blood-brain barrier. Cold Spring Harb. Perspect. Biol. *7*, a020412. https://doi.org/10.1101/cshperspect.a020412.
39. Heithoff, B.P., George, K.K., Phares, A.N., Zuidhoek, I.A., Munoz-Ballester, C., and Robel, S. (2021). Astrocytes are necessary for blood-brain barrier maintenance in the adult mouse brain. Glia *69*, 436–472. https://doi.org/10.1002/glia.23908.
40. Ralay Ranaivo, H., and Wainwright, M.S. (2010). Albumin activates astrocytes and microglia through mitogen-activated protein kinase pathways. Brain Res. *1313*, 222–231. https://doi.org/10.1016/j.brainres.2009.11.063.
41. Hyman, B.T., Van Hoesen, G.W., Kromer, L.J., and Damasio, A.R. (1986). Perforant pathway changes and the memory impairment of Alzheimer's disease. Ann. Neurol. *20*, 472–481. https://doi.org/10.1002/ana.410200406.
42. Gómez-Isla, T., Price, J.L., McKeel, D.W., Jr., Morris, J.C., Growdon, J.H., and Hyman, B.T. (1996). Profound loss of layer II entorhinal cortex neurons occurs in very mild Alzheimer's disease. J. Neurosci. *16*, 4491–4500. https://doi.org/10.1523/JNEUROSCI.16-14-04491.1996.
43. Ng, P.Y., Zhang, C., Li, H., and Baker, D.J. (2023). Senescent Microglia Represent a Subset of Disease-Associated Microglia in P301S Mice. J. Alzheimers Dis. *95*, 493–507. https://doi.org/10.3233/JAD-230109.
44. Brelstaff, J.H., Mason, M., Katsinelos, T., McEwan, W.A., Ghetti, B., Tolkovsky, A.M., and Spillantini, M.G. (2021). Microglia become hypofunctional and release metalloproteases and tau seeds when phagocytosing live neurons with P301S tau aggregates. Sci. Adv. *7*, eabg4980. https://doi.org/10.1126/sciadv.abg4980.
45. Karabag, D., Scheiblich, H., Griep, A., Santarelli, F., Schwartz, S., Heneka, M.T., and Ising, C. (2023). Characterizing microglial senescence: Tau as a key player. J. Neurochem. *166*, 517–533. https://doi.org/10.1111/jnc.15866.
46. Sharpless, N.E., Bardeesy, N., Lee, K.H., Carrasco, D., Castrillon, D.H., Aguirre, A.J., Wu, E.A., Horner, J.W., and DePinho, R.A. (2001). Loss of p16Ink4a with retention of p19Arf predisposes mice to tumorigenesis. Nature *413*, 86–91. https://doi.org/10.1038/35092592.
47. Love, M.I., Huber, W., and Anders, S. (2014). Moderated estimation of fold change and dispersion for RNA-seq data with DESeq2. Genome Biol. *15*, 550. https://doi.org/10.1186/s13059-014-0550-8.
48. Subramanian, A., Tamayo, P., Mootha, V.K., Mukherjee, S., Ebert, B.L., Gillette, M.A., Paulovich, A., Pomeroy, S.L., Golub, T.R., Lander, E.S., et al. (2005). Gene set enrichment analysis: a knowledge-based approach for interpreting genome-wide expression profiles. Proc. Natl. Acad. Sci. USA *102*, 15545–15550. https://doi.org/10.1073/pnas.0506580102.
49. Baker, D.J., Perez-Terzic, C., Jin, F., Pitel, K.S., Niederländer, N.J., Jeganathan, K., Yamada, S., Reyes, S., Rowe, L., Hiddinga, H.J., et al. (2008). Opposing roles for p16Ink4a and p19Arf in senescence and ageing caused by BubR1 insufficiency. Nat. Cell Biol. *10*, 825–836. https://doi.org/10.1038/ncb1744.
50. Conrad, C.D., Lupien, S.J., Thanasoulis, L.C., and McEwen, B.S. (1997). The effects of type I and type II corticosteroid receptor agonists on exploratory behavior and spatial memory in the Y-maze. Brain Res. *759*, 76–83. https://doi.org/10.1016/s0006-8993(97)00236-9.
51. Allen, K., Gil, M., Resnik, E., Toader, O., Seeburg, P., and Monyer, H. (2014). Impaired path integration and grid cell spatial periodicity in mice lacking GluA1-containing AMPA receptors. J. Neurosci. *34*, 6245–6259. https://doi.org/10.1523/JNEUROSCI.4330-13.2014.
52. Deacon, R.M.J. (2006). Assessing nest building in mice. Nat. Protoc. *1*, 1117–1119. https://doi.org/10.1038/nprot.2006.170.

STAR★METHODS

KEY RESOURCES TABLE

REAGENT or RESOURCE	SOURCE	IDENTIFIER
Antibodies		
mouse IgG1 anti-phospho-tau (AT8)	Thermofisher	Cat# MN1020; RRID: AB_223647
mouse IgG1 anti-tau (HT7)	Thermofisher	Cat# MN1000; RRID: AB_2314654
chicken anti-GFAP	Abcam	Cat# ab4674; RRID: AB_304558
rabbit anti-iba1	Novus	Cat# NBP2-19019; RRID: AB_3073939
rat IgG2b anti-cd11b (5C6)	Biorad	Cat# MCA711G; RRID: AB_321292
rat IgG2a anti-cd31 (MEC 13.3)	BD Pharmingen	Cat# 553370; RRID: AB_394816
goat anti-cd13	R&D	Cat# AF2335; RRID: AB_2227288
rabbit anti-aquaporin-4	Novus	Cat# NBP1-87679; RRID: AB_11006038
chicken anti-albumin	Abcam	Cat# ab106582; RRID: AB_10888110
rat IgG2a anti-Ly6C (ER-MP20)	Thermofisher	Cat# MA1-81899; RRID: AB_934514
rat IgG2a anti-CD68 (FA-11)	Novus	Cat# NBP2-33337; RRID: AB_3284937
Chemicals, peptides, and recombinant proteins		
sodium lauroyl sarcosine	MP Biomedicals	Cat# 194009
TrueBlack	Biotium	Cat# 23007
cresyl violet (acetate)	MPBio	CAS ID: 10510-54-10
GSL 1 Isolectin B4, fluorescein	Vector Laboratories	Cat# FL-1201-.5
Critical commercial assays		
QIAshredder	Qiagen	Cat# 79656
RNeasy Mini Kit	Qiagen	Cat# 74104
senescence β-galactosidase staining kit	Cell Signalling	Cat# 9860S
Deposited data		
Bulk RNA sequencing dataset	This study	GEO: GSE294816
Experimental models: Organisms/strains		
Mouse: PS19: B6;C3-Tg(Prnp-MAPT*P301S)PS19Vle/J	The Jackson Laboratory	RRID: IMSR_JAX:008169
Mouse: p16–/–: FVB.129-*Cdkn2a*$^{tm2.1Rdp}$/Nci	NCI Mouse Repository: Frederick National Laboratory	RRID: IMSR_NCIMR:01XE4
Mouse: Tie2cre: B6.Cg-Tg(Tek-cre)1Ywa/J	The Jackson Laboratory	RRID: IMSR_JAX:008863
Mouse: p16fl/fl: *Cdkn2a*$^{tm1.1Gsu}$/J	The Jackson Laboratory	RRID: IMSR_JAX:036933
Mouse: Ai14: B6.Cg-*Gt(ROSA)26Sor*$^{tm14(CAG-tdTomato)Hze}$/J	The Jackson Laboratory	RRID: IMSR_JAX:007914
Oligonucleotides		
See Table S1 for oligonucleotide sequences		N/A
Software and algorithms		
Prism (Version 10.4.2)	GraphPad	commercially available
Fiji ImageJ (Version 2.9.0/1.53t)	Fiji	open source download
R (Version 4.3.1)	CRAN	open source download
R studio (Version 2023.09.1+494)	posit	open source download
Topscan	CleverSysInc	commercially available
Ethovision XT	Noldus	commercially available

EXPERIMENTAL MODEL

Hemizygous *MAPT* ^{P301S} *PS19* (*PS19*) mice were purchased from the Jackson Laboratory (stock #008169) and maintained on a C57BL/6N genetic background at our mouse facility.[12] *PS19* mice used in this study had been backcrossed to C57BL/6N mice for at least 14 generations. *p16*^{Ink4a} (*p16*) knockout mice (FVB.129-*Cdkn2a*$^{tm2.1Rdp}$/*Nci*, strain #01XE4) were obtained from the

NCI Mouse Repository Frederick National Laboratory and similarly back crossed to C57BL/6N for at least 10 generations.[46] Genotyping for *PS19* and *p16* was performed as detailed by the Jackson Laboratory and Fredrick National Laboratory, respectively. Hemizygous *PS19* mice were bred with $p16^{-/-}$ mice to generate hemizygous *PS19*;$p16^{+/-}$ animals that were bred to $p16^{+/-}$ mice to generate the experimental $p16^{+/+}$, $p16^{-/-}$, *PS19*;$p16^{+/+}$, and *PS19*;$p16^{-/-}$ mouse cohorts. For the cell-type specific knockout of *p16* in Tie2(+) cells, $Tie2^{cre}$ (Jax stock #008863) mice were backcrossed to C57BL/6N mice for at least 5 generations. p16-floxed mice (Jax stock #036933) were backcrossed to C57BL/6N for at least 5 generations. Ai14 reporter mice (Jax stock #007914) were backcrossed to C57BL/6N for at least 5 generations and bred to our cohort of $p16^{fl/fl}$ mice to double homozygosity. Hemizygous $Tie2^{cre}$ mice were bred onto a $p16^{fl/fl}$ background and then crossed onto a *PS19* mouse background. Finally, $Tie2^{cre}$;$p16^{fl/fl}$;*PS19* mice were bred to $p16^{fl/fl}$;Ai14/Ai14 mice to generate experimental mice that were hemizygous or null for cre and *PS19* transgenes, homozygous for *p16*-floxed alleles, and heterozygous for the Ai14 allele. Animals were housed in pathogen-free barrier facility on a 12 hr light/dark cycle as described in detail previously.[11] All animal procedures were reviewed and approved by the Mayo Clinic Institutional Animal Care and Use Committee.

METHOD DETAILS

Statistical analysis

Graphpad's prism software was used for all statistical analysis. For analyses between two groups, the unpaired, two-sided t-test with Welch's correction was used. For analyses containing more than three groups, the one-way ANOVA with Tukey's multiple comparisons test was used in all cases where data were normal and sample sizes were similar across groups. Non-normal data such as those found in Figure S3G were analyzed with the non-parametric Kruskal-Wallis with Dunn's multiple comparisons test. All statistical tests are indicted in the relevant figure legends. We note that no power calculations were used. Sample sizes are based on previously published experiments in which differences were observed. No samples were excluded. Investigators were blinded to allocation during experiments and outcome assessment, except for rare instances in which blinding was not possible. Due to the large number of samples and size constraints of tests, some experiments were performed in one sex at a time and analyzed separately to prevent interference from inter-experimental variably. Where reasonable, data from both sexes is presented together. Sex and age are indicated in the y-axis of graphs and in the figure legends.

Bulk RNA Sequencing

Mice were deeply anesthetized via intraperitoneal injection of a ketamine:xylazine mixture then transcardially perfused with ice-cold phosphate-buffered saline (PBS; pH 7.4) until fluid runoff was clear. Brains were extracted, microdissected in D-PBS, and snap frozen in liquid nitrogen. RNA was extracted from the left hippocampus using the QIAshredder (Qiagen #79656) and Qiagen RNeasy Mini kit (Catalog # 74104) according to the manufacturer's instructions, then sent on dry ice to Azenta Life Sciences for next generation standard RNA sequencing (Illumina, 2x150bp, ~350M PE reads, single index). Differential expression analysis was performed using the DESeq2 R package with default parameters.[47] Gene set enrichment analysis (GSEA) software was used for pathways analysis.[48] For GSEA, gene lists and $\log_2$FCs from DESeq2 analysis were used to query gene sets form MSigDB. For gene ontology (GO) analysis, differentially expressed genes ($|\log_2 FC|>1$ and padj<0.05 by DESeq2) from relevant comparisons were input in the PantherDB tool, filtered by parent term, and clustered by functional pathways. Heatmaps were generated in Graphpad's Prism software.

Quantitative PCR

RNA extraction, cDNA synthesis and analysis were performed as previously described.[49] Primers for $p16^{Ink4a}$, $p19^{Arf}$, *p21*, *Pai1*, *Il-6*, *Il-1b*, *Cd11b, GFAP, S100β, and Tbp* were as previously described.[12] Expression of total human tau of *PS19* mice was determined using the following primers: for-5'-TGCTTTTACTGACCATGCGA-3', rev-5'-AAGACCAAGAGGGTGACACG-3'. Expression for all analysis was normalized to expression of *Tbp*. See Table S1 for all primer sequences.

Senescence-associated β-galactosidase Staining

Mice were transcardially perfused with ice-cold phosphate-buffered saline (PBS; pH 7.4) until fluid runoff was clear. This was followed by perfusion with 4% paraformaldehyde (PFA) for 10 minutes at a rate of 3 ml per minute, and then ice-cold PBS was perfused again for 2 minutes at the same rate to remove the remaining fixative. Samples were sectioned into 30-μM-thick coronal sections and stored in antifreeze solution (300 g sucrose, 300 ml ethylene glycol, 500 ml PBS) at -20°C. Sections were then incubated in SA-β-Gal staining solution per manufacturer instructions (Cell Signaling #9860) at 37°C for 10 hours. The number of SA-βgal(+) cells was counted in 2-3 tissue sections per mouse and normalized to the length of hippocampus quantified. N=2 independent experiments normalized to intraexperiment wildtype controls to account for interexperimental variability. All images were blinded prior to quantification.

Western blotting for soluble and sarkosyl insoluble proteins

Total cortex and hippocampus were freshly isolated from individual mice, weighed and homogenized in 5X volume of Buffer I (50 mM Tris base [pH 7.4], 50mM NaCl, 1mM EDTA, 1mM PMSF, 1X Halt™ Protease and Phosphatase Inhibitor Cocktail [Thermo 1861284]).

250μl of the homogenate was then added to an equal volume of Buffer S (50 mM Tris [pH 8.0], 274 mM NaCl, 5 mM KCl, 1 mM PMSF, 1X Halt™ Protease and Phosphatase Inhibitor Cocktail [Thermo 1861284]) and ultracentrifuged at 150,000g for 15 minutes at 4°C. The supernatant (S1-soluble protein fraction) was transferred to a new tube and the pellet homogenized in 3x volume of sucrose buffer (10 mM Tris [pH7.4], 0.8M NaCl, 10% sucrose, 1mM EGTA, 1 mM PMSF) before being ultracentrifuged at 150,000g for 15 minutes at 4°C. The pellet was discarded and the supernatant incubated with Sarkosyl (Sodium lauroyl sarcosinate, MP Biomedicals #194009) at a final concentration of 1% for 1 hour at 37°C. Following incubation, the samples were ultracentrifuged at 150,000g for 30 minutes at 4°C. The supernatant was discarded and the pellet was re-suspended in 25ul Buffer F (10 mM Tris [pH8], 1mM EDTA) to get the insoluble protein fraction (S2). Equal parts of 2x laemmli buffer (Bio-Rad #1610737) containing 5% β-mercaptoethanol was added to each fraction (S1 and S2) and boiled at 100°C for 15 minutes to prepare the sarkosyl soluble and insoluble protein lysates. For total protein lysate, 90ul of the homogenate (half brain in 5X volume Buffer I) was added to 110ul of Buffer T (2% SDS, 50 mM Tris [pH7.4], 274 mM NaCl, 5 mM KCl, 5mM EDTA, 1% Triton-X-100, 1 mM PMSF, 100 X Halt™ Protease and Phosphatase Inhibitor Cocktail [Thermo 1861284]). The samples were then centrifuged at 16,000g for 15 minutes at 4°C to remove debris. The supernatant was removed and added to equal parts 2x laemmli buffer with 5% β-mercaptoethanol and boiled at 100°C for 15 minutes to prepare the total protein lysate. Western blotting was performed as previously described.[11] Blots were probed with antibodies for total *tau* (ThermoFisher; MN1000, 1:5000) and phospho-*tau* (ThermoFisher; MN1020, 1:1000). Ponceau S staining was performed to normalize lysate loading for the total and S1 fraction lysates. Quantification (mean grayscale intensity) was performed on 8-bit grayscale images of blots in ImageJ (2.9.0/1.53t).

Immunofluorescence

Tissue sections were obtained as described above. Free-floating coronal brain sections were permeabilized with 0.5% Triton in tris-buffered solution with 0.5% tween-20 (TBS-T) for 1 hour at room temperature, blocked with 5% BSA in TBS-T for 30 minutes at room temperature, incubated in primary antibodies diluted in blocking buffer [chicken anti-GFAP (Abcam ab4674, 1:1000), rabbit anti-iba1 (Novus NBP2-19019, 1:1000), rat anti-cd11b (BioRad MCA711G, 1:200), rat anti-cd31(BD Pharmingen 553370, 1:500), Goat anti-cd13 (R&D Systems AF2335, 1:100), rabbit anti-aqp4 (Novus NBP1-87679), chicken anti-albumin (Abcam ab106582 1:500), mouse IgG1 anti-pTau (AT8) (Invitrogen MN1020, 1:500), mouse IgG1 anti-tau (HT7) (Invitrogen MN1000, 1:500), isolectin GS-IB4-Fluorescein (Vector Labs FL-1201, 1:250), rat anti-Ly6C (Thermofisher MA1-81899, 1:500), rat anti-CD68 (Novus NBP2-33337, 1:500)] for 15-18 h at 4 °C then in secondary antibodies at 1:500 diluted in PBS for 2 h at room temperature. Sections were mounted on glass slides, counter-stained with Dapi for 20 min, quenched for autofluorescence with Trueblack (Biotum # 23007) diluted 1:50 in 70% ethanol, rinsed in water, cover slipped in aqueous-based mounting media, and imaged on a Zeiss LSM 880 confocal system using multi-track configuration. Mean fluorescence intensity (MFI) measurements were performed on 16-bit sum-projected z-stacks (z=20) using ImageJ (2.9.0/1.53t) software. Representative images are max-projected z-stacks (z=20 or 25). Glial cell counts were performed manually on blinded 20X images.

Nissl Staining

Nissl staining was performed on coronal brain sections collected as described above. Sections between Bregma -2.5 and -2.8 were matched based on anatomical features (i.e.-the shape of the granular cell layer of the dentate gyrus) and mounted on glass slides, dehydrated in methanol for 5 min, then stained in 0.1% cresyl violet solution [0.1g cresyl violet, 300 μL glacial acetic acid, 100 mL dH_2O] for 5 min. Slides were then rinsed in DI H_2O until runoff cleared then dipped in 1% acetic acid 20 times and water 5 times. The sections were then dehydrated in an increasing gradient of ethanol and histoclear and then sealed with cytoseal and a coverslip. Brightfield images were taken on an Olympus BX63 microscope and area measurements were made by manually tracing structures of interest in ImageJ software (2.9.0/1.53t) in 2 blinded tissue sections per mouse.

Hindlimb Clasping Scoring

Hindlimb clasping was scored blinded to genotype on a scale of 0-4 in integers. Mice were picked up by their tail and suspended in air for 5 seconds while observing their hind limbs. Below are the scoring criteria.

0 – Hindlimbs remain at an angle greater than 90° apart.
1 – Hindlimbs exhibit an angle less than 90°, but do not cross the body line.
2 – Hindlimbs are parallel to body line.
3 – Hindlimbs cross inside the body line but do not touch each other.
4 – Hindlimbs cross inside the body line and physically touch or clasp each other.

Cued Fear Conditioning

For cued fear conditioning, mice learned to associate a conditioned stimulus (CS; light and tone cue) with an aversive stimulus (mild foot shock; unconditioned stimulus, US) enabling testing for amygdala-dependent cued fear conditioning. Conditioned fear was measured as freezing behavior. Specific training parameters were as follows: tone duration is 30 s; level is 70 dB, 2 kHz; shock duration is 2 s; intensity is 0.6 mA. This intensity is not painful and can easily be tolerated but will generate an unpleasant feeling. More

specifically, in the conditioning phase on day 1, each mouse was placed in a fear-conditioning chamber and allowed to explore for 2 min before delivery of a 30-s tone (70 dB) and light cue ending with a 2-s foot shock (0.6 mA). Two minutes later, a second CS-US pair was delivered. On day 2, during a priming phase, each mouse was first placed in the fear-conditioning chamber containing the same exact context, but with no CS or foot shock for a period of three minutes. One hour later, the mice were placed in a new context containing a different cleaning solution, floor texture, chamber walls and shape for the testing phase. Animals were allowed to explore for 2 min before being re-exposed to the CS alone, then again 2 min later. Freezing was analyzed for 0-120 seconds (No-Stimulus 1 (NS-1)), 120-150 seconds (CS-1), 150-170 seconds (NS-2), and 170-200 seconds (CS-2). Freezing was measured using a FreezeScan video tracking system and software (Cleversys, Inc) and displayed as percent time frozen during CS-1+CS-2, normalized to percent time frozen during NS-1 to account for locomotor differences.

Y-maze

Y-maze was adapted from a previous study.[50] Briefly, mice were habituated to the room at least one hour prior to testing. The Y-maze apparatus had three identical arms spaced apart at 120° angles with walls 20 cm tall. Mice were placed in one arm of the maze and allowed to explore the maze for 5 minutes. The sequence of arms the mouse visited was recorded and reported as total number of alternations and percent spontaneous alternations. The maze was wiped clean with hydrogen peroxide wipes in between each trial to clear any scent cues. Animal tracking was carried out using Noldus Ethovision XT.

L-maze

The L-maze was adapted from a previous study.[51] During the training phase, the mouse was guided in a clear beaker from the center of the circular table to the escape hole. For the conditioning phases, the L-maze apparatus was then placed on top of the circular table and consisted of one short arm (30 cm) connected to one long arm (60 cm) at a 90° angle. During the 5 conditioning phases each 15-20 minutes apart, the mouse was released from a start box at the end of the short arm of the L-maze, given 90 seconds to travel along the short arm, turn 90°, travel down the long arm, and enter the escape hole. If a mouse did not complete the maze in 90 seconds, they were guided to the escape hole. During the testing phase, the L-maze apparatus was removed from the circular table and a mouse was placed in the starting position. Animal tracking was carried out using Noldus Ethovision XT to calculate the heading angle of the mouse to the escape hole as an average over the first 10 cm the mouse traveled. Bright lights illuminated the table to motivate escape and a white noise machine was played constantly to muffle any sound-based spatial cues. The circular table and L-maze apparatus were also placed behind a black curtain to remove any spatial cues. The maze was wiped clean with hydrogen peroxide wipes in between each trial to clear any scent cues.

Nestlets

The nest-building test was performed as previously described.[52] Briefly, mice were habituated to the testing room the morning of testing and given one square nestlet in their home cage for the day. One hour before the dark cycle, mice were single-housed in a cage devoid of other nesting materials save for one pre-weighed square cotton fiber nestlet. Mice were left undisturbed for 16 hours. Nests were then scored on a scale from 1-5 as previously described[52] and untorn portions of the nestlet were weighed.

Vessel Diameter Measurement

Average blood vessel diameter and density were measured from coronal brain sections stained for CD31 as described under immunofluorescence using the Vessel Analysis plugin in ImageJ. Measurements were averaged from 3 tissue sections imaged at 20X magnification (3 independent experiments) per mouse and normalized to the wildtype average of each experiment to account for inter-experimental variability in staining. Representative images of the staining are 40X for better visualization.